



Title	Multi-faceted digital pyramid wavefront sensor
Authors(s)	Akondi, Vyas, Castillo, Sara, Vohnsen, Brian
Publication date	2014-07-15
Publication information	Akondi, Vyas, Sara Castillo, and Brian Vohnsen. "Multi-Faceted Digital Pyramid Wavefront Sensor." Elsevier, July 15, 2014. https://doi.org/10.1016/j.optcom.2014.03.004 .
Publisher	Elsevier
Item record/more information	http://hdl.handle.net/10197/13061
Publisher's statement	This is the author's version of a work that was accepted for publication in Optics Communication. Changes resulting from the publishing process, such as peer review, editing, corrections, structural formatting, and other quality control mechanisms may not be reflected in this document. Changes may have been made to this work since it was submitted for publication. A definitive version was subsequently published in Optics Communication (323, pp. 77-86, (2014)) https://doi.org/10.1016/j.optcom.2014.03.004
Publisher's version (DOI)	10.1016/j.optcom.2014.03.004

Downloaded 2025-12-04 23:04:04

The UCD community has made this article openly available. Please share how this access benefits you. Your story matters! (@ucd_oa)



© Some rights reserved. For more information

Multi-faceted digital pyramid wavefront sensor

Vyas Akondi*, Sara Castillo, and Brian Vohnsen

Advanced Optical Imaging Group, School of Physics, University College Dublin, Belfield, Dublin 4, Ireland

**vyas.akondi@ucd.ie*

Abstract

The modulated pyramid wavefront sensor is known for its high sensitivity and adjustable dynamic range. The need for mechanically moving parts in a modulated pyramid wavefront sensor can be overcome by using the recently proposed digital pyramid wavefront sensor. In this paper, a digital multi-faceted pyramid wavefront sensor is demonstrated with the use of a reflecting phase-only spatial light modulator. The four-pupil digital pyramid wavefront sensor with 4-facets is extended to 6 and 8-facets. It is noted from the experiments performed under identical low-noise conditions that the performance of the wavefront sensor in terms of the root mean square wavefront error remains nearly the same in cases of four, six and eight pupil configurations. Under the circumstances elucidated here, the results of simulations indicate that in the presence of scatter noise, the pyramid wavefront sensor with greater number of pupils could lead to an improvement over the standard four-pupil pyramid wavefront sensor. Noise from scattering makes the choice of optimal modulation radius critical while sensing in open-loop adaptive optics systems.

Keywords: pyramid wavefront sensor, wavefront sensing, adaptive optics, noise, Hartmann-Shack wavefront sensor, spatial light modulator.

1. Introduction

In comparison with a Hartmann-Shack (HS) wavefront sensor [1], the pyramid wavefront sensor is known for its high sensitivity, adjustable dynamic range and an ability to obtain images of higher contrast [2, 3], similar to the curvature wavefront sensor [4]. In an aberration-free system, the four facets of a conventional pyramid wavefront sensor deflect the aberrated light beam at the focal plane into four identical pupils. The introduced phase distortions can be reconstructed from the 'x' and 'y' wavefront slopes, which are proportional to the *sine* of a linear combination of the normalized pupil intensities [5]. To achieve greater dynamic range and sufficiently effective open-loop operation of the wavefront sensor, there is a need to modulate the light beam with respect to the pyramidal prism [2, 6]. The recently proposed digital pyramid wavefront sensor eliminates the need for mechanically moving parts while accommodating modulation, as required in the case of its conventional counterpart [7]. Also, the modulation amplitude can be tuned with ease to attain greater control over sensitivity and dynamic range. Another feature of the digital pyramid wavefront sensor is that the number of facets can be chosen at will to alter the number of pupil images. Related, the roof sensor [8] is yet another modification to the conventional pyramid wavefront sensor, designed to reduce the diffraction effects.

Most common noise sources in wavefront sensors are photon noise, readout noise and scattering noise. Photon noise is the fundamental uncertainty associated with light quantization. Readout noise is usually associated with photon counting ability of detectors and the error involved in converting incident photons to image pixel values. Scattering noise is an external noise that essentially originates from random scatters or in imaging applications where scattering noise from targets is unavoidable [9]. The HS wavefront sensor can be severely affected by noise. An appropriate centroiding algorithm is necessary to precisely estimate the location of HS spots, required to estimate the wavefront accurately [10]. In contrast, the curvature wavefront sensor is less affected by uniform noise [4]. This paper addresses through simulations, the effects of noise in a multi-faceted pyramid wavefront sensor in comparison with its conventional four-pupil counterpart.

An increase in the number of pupils would have a direct influence on the impact of noise and may help to overcome the adverse effects of noise on the accuracy of wavefront sensing in certain applications. The aim of this paper is to

demonstrate the feasibility of implementing six-faceted and eight-faceted digital pyramid wavefront sensors using an 8-bit reflecting spatial light modulator and thereby investigate the influence of the increased number of pupils on the performance of the wavefront sensor, in the presence of noise. Adopting a circular modulation scheme, a discussion on the optimum modulation amplitude required to achieve good results in the presence of noise is presented. In order to attain good wavefront sensing accuracy, the aberrated point spread function should be centered precisely on the pyramidal phase addressed on the SLM. A small misalignment near the focal plane could lead to a significant wavefront error analogous to a tilt aberration. A least-square fitting based modal decomposition based on Zernike polynomials is performed after following a zonal-based wavefront reconstruction procedure. This helps in eliminating tilt-offset errors.

2. Experimental setup

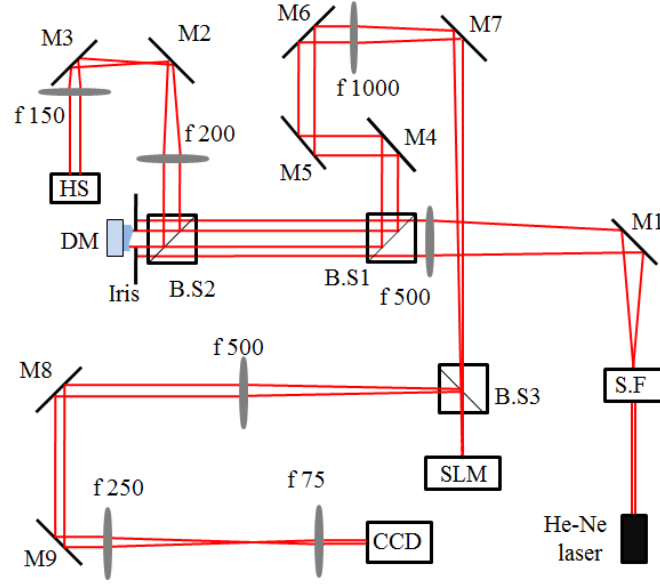


Figure 1: Schematic of the optical layout for comparison of six and eight pupil configurations with the four pupil digital pyramid wavefront sensor. All the lenses used here are achromatic doublets. S.F is a spatial filter setup, M(1-9) are mirrors and B.S(1-3) are beam splitters. Adapted from [7].

The experimental setup is shown in Fig. 1 and is similar to that used for demonstrating the working of a four-faceted digital pyramid wavefront sensor earlier [7]. A spatially filtered and collimated linearly-polarized He-Ne laser (5 mW) was used as source of light. Phase aberrations were introduced in the front focal plane of a 1000 mm focal length achromatic lens using a 140-actuator deformable mirror (DM) from Boston MicromachinesTM. This long focal length lens was required to avoid overlapping diffraction orders of the pupil images. The SLM (Hamamatsu, LCOS SLM X10468 with a pixel pitch of 20 μm) was placed one meter away from this lens such that the unaberrated light beam focuses on the SLM display. With the help of a beam splitter, the SLM reflected pupil images (four, six or eight) were captured on a CCD camera. Wavefronts are estimated from the pupil images by adopting the reconstruction approach described in the next section. Concurrently, the aberrations introduced by the DM were sensed using a commercial HS wavefront sensor. The active beam diameter is 4 mm.

3. Simulations

3.1. Pyramidal phase

Different methods have been used for simulating pyramidal phase in the case of 4-facet pyramid wavefront sensor earlier [7, 11–13]. Here, a geometric approach similar to the phase mask approach adopted by Carbillet, et. al. [13]

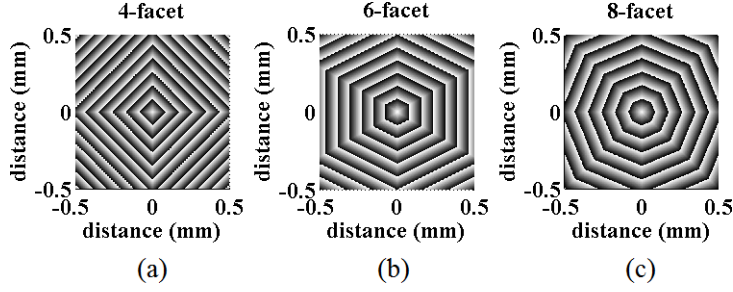


Figure 2: Wrapped phase addressed on the SLM to generate (a) 4-pupil (b) 6-pupil and (c) 8-pupil pyramid wavefront sensors is shown here. It is to be noted that the phase is over an area of 1 mm^2 , corresponding to 50×50 pixels of the SLM. For visualization, 400×400 pixels were used here. The brightest pixel in each map corresponds to a gray value of 255 and the darkest pixel to 0 which corresponds to 3π phase modulation.

was used in all three cases for uniformity and easier simulation of 6 and 8-faceted pyramidal phases. Four, six and eight faceted pyramidal phase was generated with the SLM by addressing gray scale values as shown in Fig. 2. Although a greater number of pixels (400×400) were used to simulate the phase in Fig. 2 for perspicuity, an area of 1 mm^2 on the SLM display corresponds to 50×50 SLM pixels. The apex angle of the pyramidal prism was chosen to be $\sim 179^\circ$ such that the area occupied by the pupil images on the CCD camera is optimal. To achieve this apex angle, the pyramidal phase has to be wrapped on the SLM since the maximum non-wrapped phase amplitude of the SLM at 632.8 nm is nearly 3π radians. The high resolution of the SLM allows to safely implement phase wrapping. On the contrary, the need for wrapping the phase on the SLM with square shaped pixels makes it difficult to accurately generate the required phase maps with six and eight facets. The complexity will increase further if more facets are to be introduced. Under the extreme limit, the number of facets is infinite and is analogous to the axicon wavefront sensor [14]. The intensity as measured at the detector plane is given by,

$$I_{4,6,8}^{pyr}(x, y) = FT(FT(C(x, y).e^{i\varphi(x, y)}).e^{iP_{4,6,8}(x, y)})^2 \quad (1)$$

where $C(x, y)$ defines the circular pupil and $\varphi(x, y)$ is the introduced phase aberration. P_4 , P_6 and P_8 are the geometrically calculated pyramidal phase functions (see Fig. 2) corresponding to 4, 6 and 8-faceted pyramid wavefront sensors. Here, FT represents the fast Fourier transform. To study the effects of noise, a matrix of random numbers picked from a Gaussian distribution is added to the pupil images.

3.2. Wavefront slopes and reconstruction

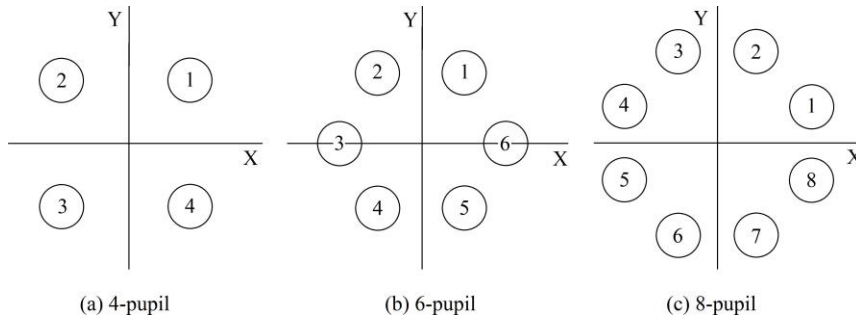


Figure 3: Location of the pupils in (a) 4-faceted (b) 6-faceted and (c) 8-faceted pyramid wavefront sensor. All the pupil images for a given case are at the same distance from the origin.

The analytical dependence of the wavefront slopes on the pupil images in cases of 4, 6 and 8-faceted pyramid wavefront sensors varies due to their fundamental geometrical distinction. Figure 3 shows the indexing of the pupil

geometry together with a reference coordinate system for the wavefront sensor signal to evaluate the relationship between the intensity in the pupils and the wavefront slopes. Following Fig. 3(a), in the 4-facet case, the wavefront slopes are defined by Eqs. (2) and (3).

$$S_x(x, y) = \frac{\xi}{f} \cdot \sin \frac{\pi}{2} \cdot \frac{I_1(x, y) - I_2(x, y) - I_3(x, y) + I_4(x, y)}{I_1(x, y) + I_2(x, y) + I_3(x, y) + I_4(x, y)} \quad (2)$$

$$S_y(x, y) = \frac{\xi}{f} \cdot \sin \frac{\pi}{2} \cdot \frac{I_1(x, y) + I_2(x, y) - I_3(x, y) - I_4(x, y)}{I_1(x, y) + I_2(x, y) + I_3(x, y) + I_4(x, y)} \quad (3)$$

Here, ξ denotes the magnitude of circular modulation and f is the focal length of the lens used for focusing the light beam on the SLM. Similarly, for 6-faceted pyramid wavefront sensor, the slopes are defined by Eqs. (4) and (5).

$$S_x(x, y) = \frac{\xi}{f} \cdot \sin \frac{\pi}{6} \cdot \frac{\sum_{j=1,5,6} I_j(x, y) - \sum_{j=2,3,4} I_j(x, y)}{\sum_{j=1}^6 I_j(x, y)} \quad (4)$$

$$S_y(x, y) = \frac{\xi}{f} \cdot \sin \frac{\pi}{6} \cdot \frac{\sum_{j=1,2} I_j(x, y) - \sum_{j=4,5} I_j(x, y)}{\sum_{j=1}^6 I_j(x, y)} \quad (5)$$

In Eq. 5, the non-symmetric contribution of the pupils to the 'x' and 'y' slopes has to be noted. This is due to the location of centers of the pupils I_3 and I_6 on the X-axis.

In the same manner, for the case of 8-faceted pyramid wavefront sensor, the slopes are given by Eqs. (6) and (7).

$$S_x(x, y) = \frac{\xi}{f} \cdot \sin \frac{\pi}{8} \cdot \frac{\sum_{j=1,2,7,8} I_j(x, y) - \sum_{j=3,4,5,6} I_j(x, y)}{\sum_{j=1}^8 I_j(x, y)} \quad (6)$$

$$S_y(x, y) = \frac{\xi}{f} \cdot \sin \frac{\pi}{8} \cdot \frac{\sum_{j=1,2,3,4} I_j(x, y) - \sum_{j=5,6,7,8} I_j(x, y)}{\sum_{j=1}^8 I_j(x, y)} \quad (7)$$

After evaluating the wavefront slopes, S_x and S_y from the obtained pupil images, the wavefronts ($\hat{\phi}$) are estimated as in Eqs. 8 and 9 using Southwell's slope geometry [7, 10, 15]:

$$\frac{S_x^{k+1,l} + S_x^{k,l}}{2} = \frac{\hat{\phi}^{k+1,l} - \hat{\phi}^{k,l}}{h}, k = 1, 2, \dots, N-1 \text{ and } l = 1, 2, \dots, N, \quad (8)$$

$$\frac{S_y^{k,l+1} + S_y^{k,l}}{2} = \frac{\hat{\phi}^{k,l+1} - \hat{\phi}^{k,l}}{h}, k = 1, 2, \dots, N \text{ and } l = 1, 2, \dots, N-1 \quad (9)$$

when $N \times N$ subapertures are used for wavefront sensing. Using matrix formulation, Eqs. 8 and 9 can be simplified to $DS = A\phi$. Here, A and D are sparse matrices. Multiplying on either side of $DS=A\phi$ with A^T and applying singularvalue decomposition technique, the estimated wavefront phase, $\hat{\phi}$ [7, 10] becomes,

$$\hat{\phi} = U\Lambda^{-1}V^T A^T DS. \quad (10)$$

3.3. Modal decomposition

It is convenient to represent the reconstructed wavefront using orthogonal Zernike modes in a closed loop adaptive optics system that involves modal wavefront correction [4]. To this end, the estimated wavefront phase is fitted with Zernike polynomials using the method of least squares such that,

$$\hat{\phi}(x, y) = \sum_{j=b_l}^{b_u} a_j Z_j(x, y), \quad (11)$$

where b_l and b_u are the lower and upper limits to the Zernike polynomial index used for representing the reconstructed wavefront respectively, a_j represents the Zernike coefficient and $Z_j(x, y)$ are the Zernike polynomials. The single index notation of the Zernike polynomials (Z_j) is extracted from the standard double index notation (Z_n^m ; ANSI standard, ANSI Z80.28) by adopting the ordering method defined as follows:

$$j = \frac{n(n+2) + m}{2} \quad (12)$$

where ' n ' is the radial index and ' m ' is the azimuthal index.

4. Results

4.1. Experimental results

Zernike aberrations of known magnitude (expressed in terms of the peak-to-valley) are introduced with the help of the DM. The pupil images for different amplitude of circular modulation corresponding to the introduced aberrations are then captured by the CCD camera for the three cases of 4, 6 and 8-faceted pyramid wavefront sensors. The wavefront slopes are thereby evaluated by using Eqs. (2) and (3) in case of 4-facets, Eqs. (4) and (5) in 6-facet case and Eqs. (6) and (7) in 8-facet case. Finally, the wavefronts are estimated using Eq. (10). The root mean square (RMS) wavefront error is calculated from the residual wavefront error, which is a difference between HS measured wavefront (φ^{HS}) and the wavefront reconstructed using the digital pyramid wavefront sensor (φ^{PWS}), by using the following expression:

$$RMS = \frac{\sqrt{\sum_{ij} (\varphi_{ij}^{HS} - \varphi_{ij}^{PWS})^2}}{N}, \quad (13)$$

where ' N ' is the total number of pixels used to represent the wavefronts φ^{HS} and φ^{PWS} .

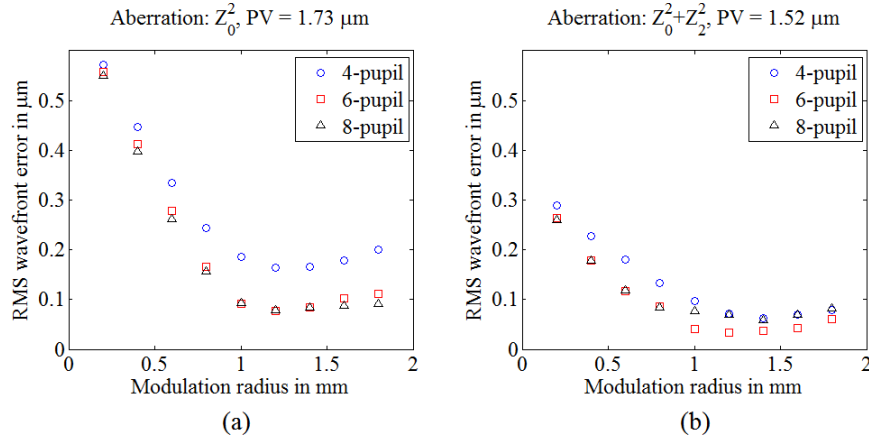


Figure 4: Experimental comparison of 4, 6 and 8-faceted pyramid wavefront sensors: estimated RMS wavefront error as a function of modulation radius while sensing (a) defocus (HS measured peak-to-valley is 1.73 μm) and (b) a combination of defocus and astigmatism aberrations (HS measured peak-to-valley is 1.52 μm).

The plots of the estimated RMS wavefront error as a function of modulation radius for four, six and eight faceted digital pyramid wavefront sensors when measuring defocus and a combination of defocus and astigmatism are shown in Fig. 4. The resultant RMS wavefront error for the four-pupil case is lower than estimated earlier [7] and this is largely due to the removal of tilt terms ($j = 1, 2$) after performing a modal decomposition based on Zernike polynomials. It was reported that the RMS wavefront error decreases with increasing modulation radius and then increases again beyond a certain modulation radius. This increase is attributed to the tilt caused due an offset between

the center of the pyramid apex and the point spread function. Eliminating the tilt coefficients after zonal wavefront reconstruction helped in reducing the effects of the tilt offset while sensing, clearly evident from Fig. 2. However, the predicted RMS wavefront error increases by a very small amount after a minimal RMS wavefront error. This is attributed to the overestimation of the magnitude of the wavefront aberrations for higher modulation radius. Also, there is a noticeable coupling between the higher-order coefficients and the lower-order coefficients, which increases with modulation. For instance, while sensing the introduced primary defocus aberration (Z_0^2), a small but significant magnitude of spherical aberration (Z_0^4) coefficient is detected. Furthermore, while sensing primary astigmatism (Z_2^2), secondary astigmatism (Z_2^4) coefficient assumes a non-zero value.

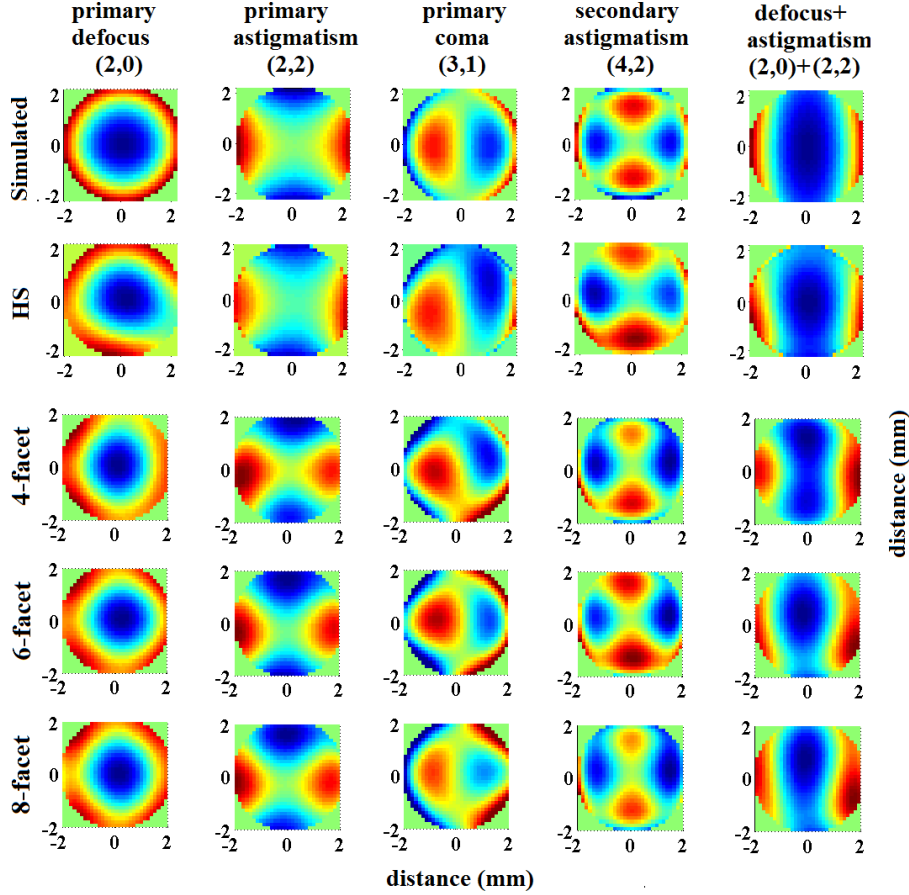


Figure 5: Experimental comparison of the wavefronts reconstructed using 4, 6 and 8-faceted pyramid wavefront sensor (modulation radius = 1.6 mm) with that measured with the HS and simulated aberrations. Here, Zernike coefficients from $j=3$ to $j=15$ were used for representing the reconstructed wavefronts.

Figure 5 shows the reconstructed wavefronts obtained using 4, 6 and 8-faceted pyramid wavefront sensors while sensing defocus (Z_0^2), astigmatism (Z_2^2), coma (Z_3^1), secondary astigmatism (Z_2^4) and a combination of astigmatism and defocus ($Z_0^2 + Z_2^2$). Here, the modulation radius was 0.8 mm. The results of wavefront sensing using the multi-faceted digital pyramid wavefront sensor are compared with the HS measurements and the simulated wavefronts. The reconstructed phase maps (Fig. 5) and the experimentally predicted RMS wavefront error plots (Fig. 4) validate the working of a multi-faceted digital pyramid wavefront sensor.

The experimental results indicate that the performance of the multi-faceted pyramid wavefront sensors is nearly the same irrespective of the number of facets. The minor differences are attributed to uncontrolled noise sources in the obtained pupil images including detector readout noise, print-through effects of DM actuator posts, erroneous SLM

amplitude modulation errors, laser noise and scattering by dust particles.

4.2. Simulation results

Simulations were performed to test the working of the multi-faceted digital pyramid wavefront sensor. The experimental conditions are prone to several uncontrolled noise sources in the pupil images and it is particularly difficult to apply noise in a controlled manner to the pupil images experimentally. Hence, a simulation based analysis of the multi-faceted pyramid wavefront sensor in the presence of noise was performed.

Simulation parameters were selected so as to match the experimental conditions closely. The beam diameter was kept at 4 mm, $f = 1$ m and 41×41 subapertures were used for wavefront reconstruction. The number of pixels used for simulating a single pupil image is 165×165 pixels. Bilinear interpolation was used to reduce the number of pixels to 41×41 and hence reduce the computational time for estimating the wavefront phase (see Eq. 10). Zernike aberrations, $\varphi(x,y) = \alpha Z_m^{pyr}(x,y)$, of a given magnitude (α) were used for the evaluation of the wavefront sensor. The intensity in the pupil plane ($I_{4,6,8}$) for the three cases of 4, 6 and 8-faceted pyramid wavefront sensor is calculated using Eq. (1).

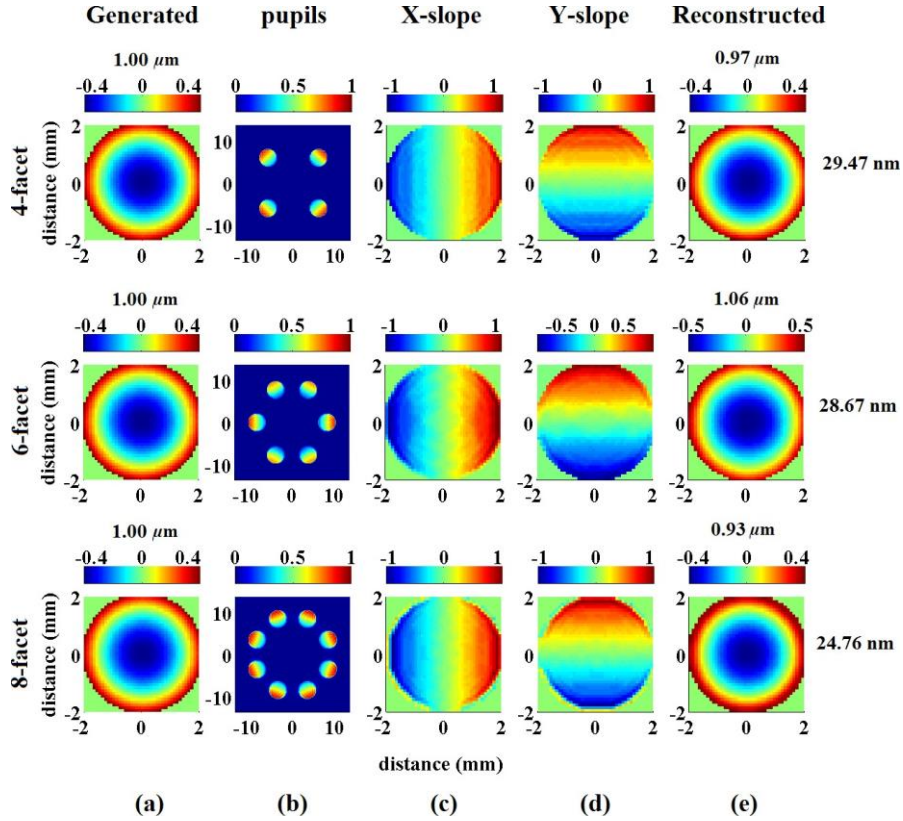


Figure 6: Simulations: demonstration of sensing primary defocus (Z_0^2) using 4, 6 and 8-faceted digital pyramid wavefront sensors. (a) Simulated phase screen with a peak-to-valley of $1.0 \mu\text{m}$; (b) pupil plane image corresponding to (a); (c) X and (d) Y wavefront slopes calculated from (b) in $\times 10^{-3}$; (e) reconstructed wavefront. The peak-to-valley of the reconstructed wavefronts is shown above sub-figures in (e) and the RMS wavefront error is shown on the right hand side. The modulation radius is 1.6 mm .

Figure 6(b) shows the normalized pupil intensity images for 4, 6 and 8-facet cases, corresponding to the introduced primary defocus aberration, shown in Fig. 6(a), with a peak-to-valley of $1 \mu\text{m}$. The corresponding 'x' and 'y' slopes of the wavefront are shown in Figs. 6(c-d). The reconstructed wavefronts are shown in Fig. 6(e). The modulation radius is 1.6 mm . It is noted that the RMS wavefront error is below $\lambda/20$. The RMS wavefront error decreases slightly with increasing number of facets. However, the decrease in the error is a mere 16% .

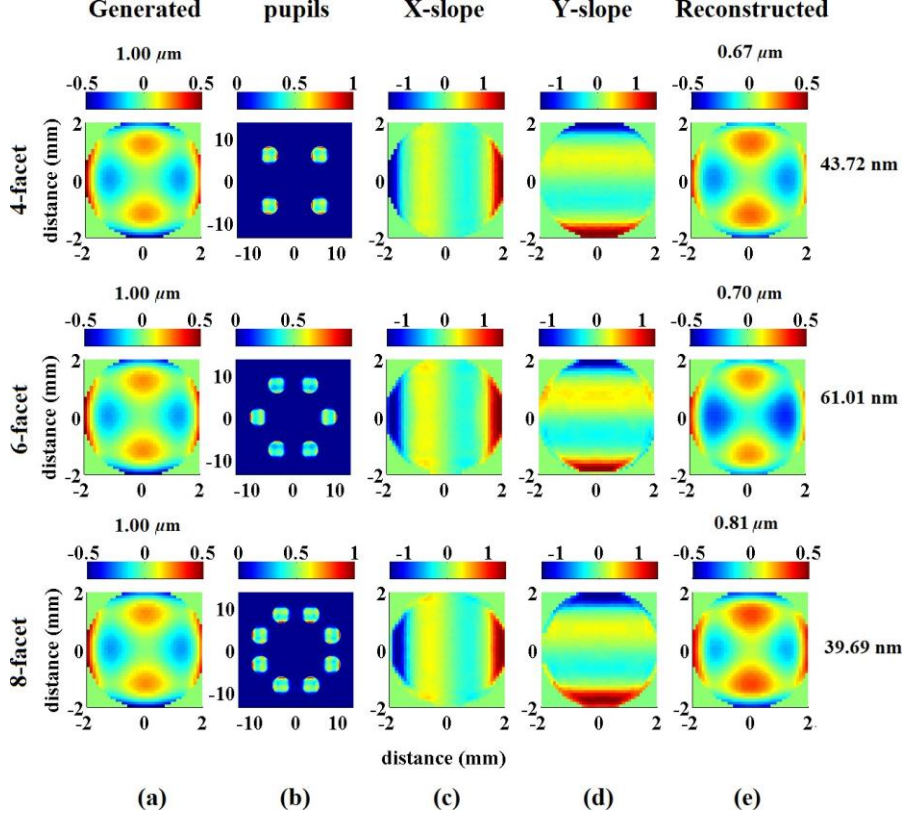


Figure 7: Simulations: demonstration of sensing secondary astigmatism (Z_2^4) using 4, 6 and 8-faceted digital pyramid wavefront sensors. (a) Simulated phase screen with a peak-to-valley of $1.0 \mu\text{m}$; (b) pupil plane image corresponding to (a); (c) X and (d) Y wavefront slopes calculated from (b) in $\times 10^{-3}$; (e) reconstructed wavefront. The peak-to-valley of the reconstructed wavefronts is shown above sub-figures in (e) and the RMS wavefront error is shown on the right hand side. The modulation radius is 1.6 mm .

When examining the RMS wavefront error for higher-order secondary astigmatism aberration (see Fig. 7), clearly the RMS wavefront error is higher when compared to that for defocus, as also noted earlier [7]. However, it is to be noted here that in the case of secondary astigmatism, the RMS error in 6-faceted pyramid wavefront sensor is $\sim 54 \%$ higher than 4-facet case and $\sim 40 \%$ higher than 8-facet case. This significant difference is due to the non-contribution of I_1 and I_6 in the calculation of ‘y’ slope in the 6-faceted pyramid wavefront sensor as seen from Eq. (5).

Considering a more complicated case of atmospheric turbulence, the Kolmogorov turbulence model and FFT based phase screen simulation method [16] were adopted to generate a sample wavefront as shown in Fig. 8(a). In this case, the 4-facet pyramid wavefront sensor performs marginally better ($\sim 29 \%$) than the other two cases. This could be due to the averaging out of the higher spatial frequencies in the phase screen while using greater number of pupil images for estimating the wavefront slopes. In cases where the high spatial frequency information in the pupil images is critical, even a minor mistake in the selection of the pupil location could significantly affect the accuracy of wavefront sensing.

Readout noise was simulated by generating a matrix of random numbers picked from a Gaussian distribution having a zero mean and standard deviation of unity. This matrix, after suitable amplification required for a given signal to noise ratio (SNR), was added to the intensity at the detector plane (see Eq. 1). The addition of readout noise (SNR = 14 dB) in the four-pupil case, while sensing defocus (Z_0^2) with a peak-to-valley of $1.5 \mu\text{m}$, increased the RMS wavefront error from 25.67 nm to $32.14 \pm 8.58 \text{ nm}$ (indicates the mean and standard deviation of 5 repetitions). It was observed that increasing the number of facets did not show any significant improvement in terms of the RMS wavefront error. Increasing the noise further to a SNR equal to unity, the RMS wavefront error increased to $135.05 \pm$

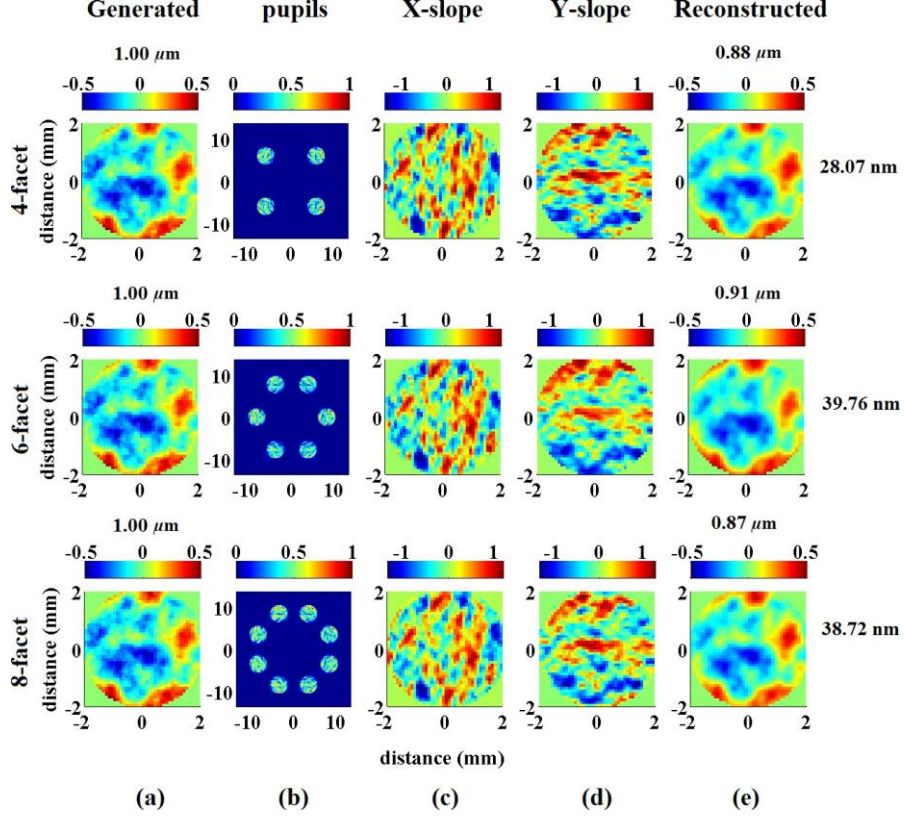


Figure 8: Simulations: demonstration of sensing an atmospheric phase screen using 4, 6 and 8-faceted digital pyramid wavefront sensors. (a) Simulated atmospheric phase screen with a peak-to-valley of $1.0 \mu\text{m}$; (b) pupil plane image corresponding to (a); (c) X and (d) Y wavefront slopes calculated from (b) in $\times 10^{-3}$; (e) reconstructed wavefront. The peak-to-valley of the reconstructed wavefronts is shown above sub-figures in (e) and the RMS wavefront error is shown on the right hand side. The modulation radius is 1.6 mm .

11.76 nm.

Certain applications require to operate the pyramid wavefront sensor in a photon noise limited regime [17]. Under these conditions, the results of simulations show that as the number of photons reaching the detector is reduced, the RMS wavefront error increases exponentially. Again, there is no significant difference in 4, 6 and 8 faceted digital pyramid wavefront sensors under conditions of photon noise alone.

In retinal imaging problems, the strength of scattering noise varies with subject under consideration and conventional wavefront sensors perform poorly under these conditions [9]. The scattering noise in the light captured at the pupil plane (see Eq. 1) could be non-uniform. An ideal approach to perform a comparative study of the performance of 4, 6 and 8 faceted pyramid wavefront sensors in the presence of scatter noise is to add uniform random noise to the same fragment of the detector pixels in all three cases and then compare the accuracy of wavefront sensing. As is the case for readout noise, it was seen that in this situation too, the performance of 4, 6 and 8 faceted pyramid wavefront sensors is indistinguishable. Alternatively, a comparison was made by adding scatter noise at the location of the first pupil (I_1) in all the three cases. To simulate such a situation in a simple manner, uniform random noise was added to the simulated detector pixels corresponding to one of the pupils alone (see Eq. 1). The wavefront slopes for 4, 6 and 8 faceted pyramid wavefront sensors are then estimated using Eqs. (2-7). The wavefronts are reconstructed using Eq. (10) and the RMS wavefront error was then estimated. However, it has to be noted that if noise is added on an area corresponding to one pupil at a random location on the detector, then, with increasing number of facets, there is greater probability that the pupils are affected by noise. Figure 9 shows a comparison of the plots of RMS wavefront error as a function of modulation radius for 4, 6 and 8-faceted pyramid wavefront sensors, while sensing defocus (Figs.

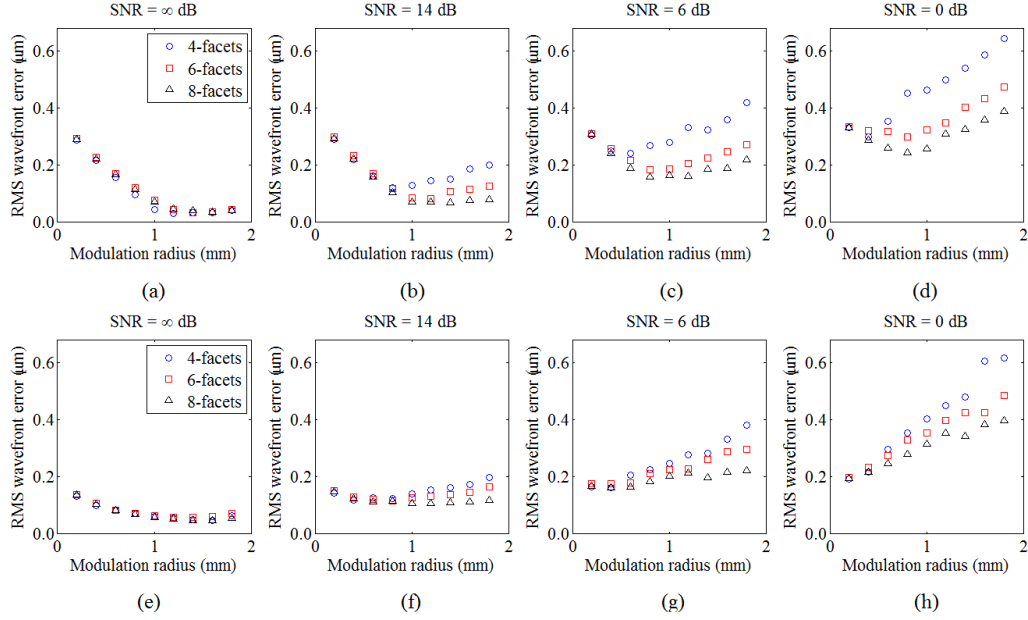


Figure 9: Simulations: comparison of the RMS wavefront error in cases of 4, 6 and 8 faceted pyramid wavefront sensors as a function of modulation radius in the presence of uniform random noise in one of the pupils, while sensing (a-d) defocus aberration and (e-h) secondary astigmatism each with a peak-to-valley of $1.80 \mu\text{m}$. Signal to Noise Ratio (SNR) measured in terms of dB is shown above each sub-figure.

9(a-d)) and secondary astigmatism (Figs. 9(e-h)), each with a peak-to-valley of $1.80 \mu\text{m}$. While sensing defocus and when $\text{SNR} = 14 \text{ dB}$, the minimum RMS wavefront error in the case of 4-faceted pyramid wavefront sensor occurs at a modulation radius of 0.80 mm and is 78 % higher than the minimum RMS wavefront error in the case of 8-faceted pyramid wavefront sensor, which occurs at a 1.4 mm modulation. The smallest modulation radius for which the RMS wavefront error is minimum, shifts to lower values in the presence of noise. The shift is lower in case of 8-facet case than for the 4-facet case. This decrease implies that the dynamic range of the wavefront sensor falls more for the 4-facet case than for 8-facet case in the presence of noise. A similar behavior was observed for lower-order aberrations ($j < 10$). A straightforward inference is that the presence of scatter noise in one of the pupils has a greater effect on the 4-facet case when compared to the 8-facet case, while sensing lower-order aberrations. However, when sensing higher-order aberrations, the minimum RMS wavefront error occurs at a low modulation radius, where the difference in the performance of 4-facet and 8-facet cases is negligible as can be seen in Figs. 9(e-h). Also, by examining the slope expressions for 4, 6 and 8-faceted pyramid wavefront sensors (see Eqs. 2-7), it can be noted that if variance is to be estimated for the calculated 'x' and 'y' slopes affected by noise, a factor of four appears in the denominator in the case of 4-faceted pyramid wavefront sensor, whereas eight in the case of 8-faceted pyramid wavefront sensor.

Figure 10 shows reconstructed phase maps in the presence of noise ($\text{SNR} = 14 \text{ dB}$) while sensing secondary astigmatism (Z_3^4) in all the three cases. The RMS wavefront error reduces significantly in 8-facet case when compared to the 4-facet pyramid wavefront sensor.

A comparison of 4 and 8-facet pyramid wavefront sensor in terms of the RMS wavefront error as a function of modulation radius while changing the magnitude of defocus aberration (Z_0^2) in the presence of noise ($\text{SNR} = 14 \text{ dB}$) is shown in Fig. 11. As the magnitude of defocus increases, the accuracy of wavefront sensing drops and the smallest modulation radius for which the RMS wavefront error is minimum shifts to higher values. In the presence of scatter noise, the RMS wavefront error increases and the optimal modulation radius increases with increasing magnitude of defocus. It can be seen that the increase in the RMS wavefront error is much lower in the 8-facet case in comparison with the 4-facet pyramid wavefront sensor. The simulations were repeated with astigmatism, coma and trefoil aberrations and it is noted that the conclusions drawn here are not affected.

Clearly, the presence of photon noise and readout noise decreases the quality of wavefront sensing in a four-pupil pyramid wavefront sensor. Increasing the number of pupil images does not improve it any further. However, it was

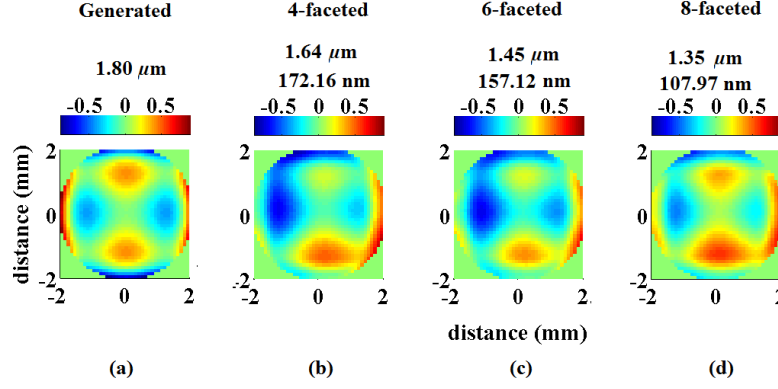


Figure 10: Simulations: a comparison of the wavefronts reconstructed in the presence of noise ($\text{SNR} = 14 \text{ dB}$) while sensing (a) $1.80 \mu\text{m}$ peak-to-valley secondary astigmatism (Z_0^2) in cases of (b) 4, (c) 6 and (d) 8 faceted pyramid wavefront sensors. The peak-to-valley (in μm) of the reconstructed wavefronts and the RMS wavefront error (in nm) is shown above each sub-figure. The modulation radius is 1.2 mm .

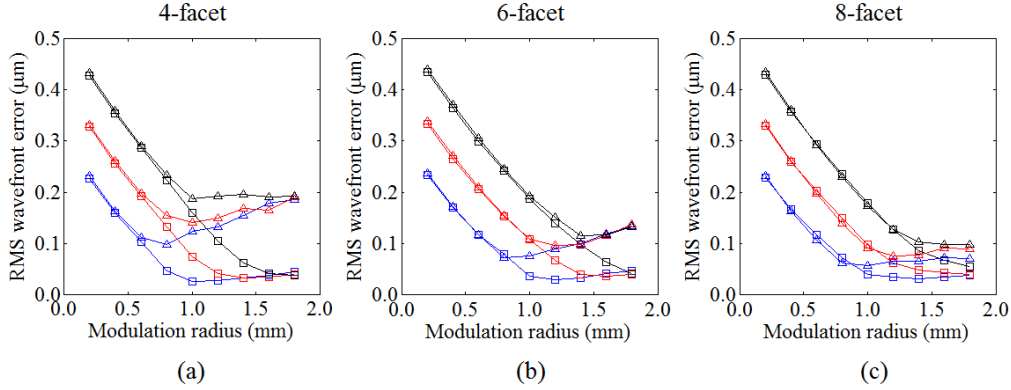


Figure 11: Simulations: a comparison of 4, 6 and 8-faceted pyramid wavefront sensor in terms of the RMS wavefront error with changing modulation amplitude for different magnitudes (Blue - $1.5 \mu\text{m}$ PV, Red - $2.0 \mu\text{m}$ PV and Black - $2.5 \mu\text{m}$ PV) of defocus aberration (Z_0^2) in the presence of noise (triangular marker: $\text{SNR} = 14 \text{ dB}$; square marker: $\text{SNR} = \infty \text{ dB}$).

observed that in the presence of scattering noise, increasing the number of pupil images helps to improve the accuracy of wavefront sensing significantly.

5. Discussion

The SLM allows the number and location of active pupils to be set at will so that problematic areas with increased scattering or camera noise may be excluded. the advantage of the SLM is that it can be swiftly reconfigured and different number of facets can be tested.

The number of pupils cannot be indiscriminately increased as sufficiently high number of camera pixels should be maintained in each. Also, this is due to the possibility of overlapping pupil images. Errors due to overlapping pupils can be overcome to a certain extent by either increasing the focal length of the lens used for focusing the light beam on the pyramid wavefront sensor or by using an SLM with a smaller pixel size. In addition, the performance of the proposed multi-faceted digital pyramid wavefront sensor is limited by the slow frame-rate and monochromatic nature of the SLM.

The modal wavefront decomposition implemented here is advantageous in closed-loop operation of the digital pyramid wavefront sensor in mode-wise wavefront correction systems. Any tilt-offset issues due to the alignment

of the pyramid apex with respect to the light beam can be largely eliminated by removing the tilt terms after modal decomposition of the reconstructed wavefront. In closed-loop adaptive optics where scattering is a concern, the choice of pupil numbers could have an effect on the rate of convergence. Nevertheless, to maintain high sensitivity in closed-loop, a lower modulation must be chosen.

While simulating noise in the case of 6-facet pyramid wavefront sensor (Figs. 9-11), it has to be noted that noise was added to the pupil that contributes to both 'x' and 'y' slopes (see Eq. (4) and Eq. (5)). Addition of noise to the pupil I_3 leads to an RMS wavefront error that is lower than for pupil I_1 .

Although a zonal wavefront reconstruction was applied here, alternatively, a modal wavefront reconstruction procedure could be used to obtain wavefront Zernike coefficients [18]. The use of zonal approach allows to retain the robustness of reconstruction from slope measurements in terms of detecting all the spatial frequencies. Increasing the number of subapertures from 41×41 to higher values did not substantially improve the accuracy of wavefront sensing.

By rotating the Cartesian grid with respect to the pupil image, it is possible to eliminate any wavefront errors that arise due to non-symmetric contributions to 'x' and 'y' slopes of the wavefront in the case of a 6-facet pyramid wavefront sensor. However, care has to be taken while evaluating the contribution of individual pupil components to the wavefront slopes. This analysis is beyond the scope of this paper. Further, it is to be investigated if the optimal choice of the number of facets should be multiples of two or powers of it. The average standard deviation in the calculation of the RMS wavefront error in Fig. 9 is $\sim 0.01 \mu\text{m}$, for ten repetitions.

Although photon noise, readout noise and scatter are independent noise sources, they generally occur in combination and the accuracy of the device would then be more complicated and hence a careful analysis has to be done on a case-by-case basis.

In conclusion, we demonstrated the working of 6-faceted and 8-faceted pyramid wavefront sensors. The use of an SLM allows easy switching between 4, 6 and 8-facet pyramid wavefront sensors.

Acknowledgements

The authors wish to thank Science Foundation Ireland for the financial support (Grants: 07/SK/B1239a and 08/IN.1/B2053).

References

- [1] R.V. Shack, J. Opt. Soc. Am. 61 (1971) 656.
- [2] R. Ragazzoni, J. Mod. Opt. 43 (1996) 289-293.
- [3] C. Verinaud, Opt. Commun. 233 (2004) 27-38.
- [4] R.M. Basavaraju, V. Akondi, S.J. Weddell, R.P. Budihal, Opt. Commun. 312 (2014) 23-30.
- [5] A. Burvall, E. Daly, S.R. Chamot, C. Dainty, Opt. Express 14 (2006) 11925-11934.
- [6] I. Iglesias, R. Ragazzoni, Y. Julien, P. Artal, Opt. Express 10 (2002) 419-428.
- [7] V. Akondi, S. Castillo, B. Vohnsen, Opt. Express 21 (2013) 18261-18272.
- [8] V. Korkiakoski, C. Verinaud, in: Y. Clenet, J.M. Conan, T. Fusco, G. Rousset (Eds.), 1st AO4ELT conference - Adaptive Optics for Extremely Large Telescopes, 2010, pp. 03007.
- [9] F.D. Dutton, A. Benito, J. Pujol, M. Arjona, J.L. Guell, P. Artal, Investig. Ophthalmol. Vis. Sci. 47 (2006) 1710-1716.
- [10] V. Akondi, B. Vohnsen, Ophthalmic Physiol. Opt. 33 (2013) 434-443.
- [11] V. Korkiakoski, C. Verinaud, M.L. Louarn, R. Conan, Appl. Opt. 46 (2007) 6176-6184.
- [12] S. Esposito, A. Riccardi, Astron. Astrophys. 369 (2001) L9-L12.
- [13] M. Carbillet, C. Verinaud, B. Femenia, A. Riccardi, L. Fini, Mon. Not. R. Astron. Soc. 356 (2005) 1263-1275.
- [14] B. Vohnsen, S. Castillo, D. Rativa, Opt. Lett. 36 (2011) 846-848.
- [15] W.H. Southwell, J. Opt. Soc. Am. 70 (1980) 998-1006.
- [16] R.M. Basavaraju, V. Akondi, R. P. Budihal, in: Proceedings of SPIE, vol. 7736, 2002, pp. 77363Z.
- [17] S.R. Chamot, C. Dainty, S. Esposito, Opt. Express 14 (2006) 518-526.
- [18] R. Cubalchini, J. Opt. Soc. Am. 69 (1979) 972-977.